Theoretical Investigation of Jahn−Teller Dynamics in the $^2E'$ Electronic Ground State of the Cyclopropane Radical Cation

T. S. Venkatesan and S. Mahapatra*

School of Chemistry, University of Hyderabad, Hyderabad, 500 046 India

L. S. Cederbaum and H. Köppel*,†

Theoretical Chemistry, Institute of Physical Chemistry, University of Heidelberg, Im Neuenheimer Feld 229, D-69120 Heidelberg, Germany

Received: November 13, 2003; In Final Form: January 14, 2004

The static and dynamic aspects of (E × e)−Jahn−Teller (JT) interactions in the electronic ground state ($\tilde{X}^2E'$) of the cyclopropane radical cation are investigated with the aid of an ab initio based quantum dynamical approach. The valence photoelectron spectrum of cyclopropane pertinent to an ionization to the $\tilde{X}^2E'$ electronic manifold of its radical cation is calculated and compared with the most recent experimental recording of Holland and co-workers using He I and synchrotron radiation as excitation sources [*J. Electron Spectrosc. Relat. Phenom.* **2002**, *57*, 125]. A model diabatic Hamiltonian up to a quadratic vibronic coupling scheme and ab initio calculated coupling parameters are employed in the quantum dynamical simulations. Despite some minor details, the theoretical results are in good accord with the observed bimodal shape of the photoelectron band. The observed splitting of the maxima of ∼0.78 eV in the bimodal profile compares well with our theoretical value of ∼0.76 eV. A strong first-order JT activity of the degenerate vibrational modes is discovered, which results in the distinct twin structure of the photoelectron band, indicating transitions to both the sheets of the so-called Mexican hat potential energy surface of the $\tilde{X}^2E'$ electronic ground state of the radical cation. Two Condon active (A_1') and three JT active (E') vibrational modes are found to contribute mostly to the nuclear dynamics in this electronic manifold. The low-energy progression in the photoelectron band is found to be mainly caused by the degenerate CH_2 wagging and ring deformation modes. While the linear vibronic coupling scheme overestimates the observed spacing in the low-energy progressions, it leads to a very good agreement with the overall shape of the observed band. The effect of quadratic coupling terms of the Hamiltonian on this low-energy progression is also discussed.

I. Introduction

The Jahn−Teller (JT) effect[1]—that a nonlinear molecule in an orbitally degenerate state spontaneously distorts to a configuration of reduced symmetry—is one of the most fascinating phenomena in chemistry. Since the classical work of Longuet−Higgins[2] on the JT effect in a doubly degenerate (E) electronic state caused by the degenerate (e) vibrational modes [the (E × e)−JT effect], much effort has been devoted to elucidate its nature and importance in a wide variety of systems including transition metal complexes,[3] solid-state physics and chemistry,[4−6] organic hydrocarbons, radicals and ions,[7−11] and fullerenes.[12] The advent of high-resolution spectroscopic measurement techniques have further motivated the invention of benchmark theoretical models[13] to better understand the static and dynamical aspects of multimode JT interactions in many other polyatomic molecular systems [see, for example, the review articles on the subject in refs 7 and 14 and the references therein].

A particularly important consequence of JT interactions is the occurrence of *conical intersections*[7,15,16] of electronic potential energy surfaces (PESs). In this situation the nuclear motion ceases to be confined to a single PES. In more general terms, a nonadiabatic situation is reached and the well-known adiabatic or Born−Oppenheimer approximation breaks down. Typically, the (E × e)−JT conical intersection (which is the main subject of this paper) exhibits a Mexican hat type of topography in the linear coupling limit—the lower potential surface comprising three equivalent minima and three equivalent saddle points linking pairs of minima and the upper one resembles a conical shape with its vertex touching the lower one at the point of 3-fold-symmetry.[17] Especially, near conical intersections the nonadiabatic coupling terms are of singular strength. In the case of multimode conical intersections this often leads to a highly diffuse spectral envelope—the vibrational levels of the upper surface are completely dissolved in the quasi-continuum of vibrational levels of the lower surface.[7] In a time-dependent picture this generally yields a femtosecond nonradiative decay of the upper electronic state.[7,13b,d,e,18]

In the present work we focus on the photoionization of cyclopropane (CP) to the electronic ground state of the cyclopropane radical cation (CP^+). The photoelectron spectrum of CP in a wide electron binding energy range has been recorded by various experimental groups using Ne I, He I, He II, and synchrotron radiation as excitation sources.[19−27] Among these, the recent 21.22 eV recording of Holland and co-workers[27] using synchrotron and He I radiation seems to be better resolved. The photoelectron band recorded by these authors in the 9−20 eV

---

* To whom correspondence should be addressed. E-mail: smsc@uohyd.ernet.in.

† E-mail: horst@tc.pci.uni-heidelberg.de.

10.1021/jp037468j CCC: $27.50

electron binding energy range revealed ionization from five outer valence orbitals of CP. The equilibrium geometry of CP in its electronic ground state belongs to the D_{3h} symmetry point group. Using the D_{3h} symmetry, the ground-state molecular orbital sequence of CP can be written as[28−32,34]

$$(1a_1')^2(1e')^4(2a_1')^2(2e')^4(1a_2'')^2(3a_1')^2(1e'')^4(3e')^4$$

The experimental photoelectron spectrum of CP[19−27] exhibits a twin band centered around ∼11 eV, a broad band at ∼13.2 eV, and two strongly overlapping bands at ∼15.7 and ∼16.5 eV. These peaks are attributed to the ionization of an electron from the 3e′, 1e″, $3a_1'$, and $1a_2''$ molecular orbitals, respectively. The peak due to the ionization from the 3e′ molecular orbital is of special interest and is examined herein. This ionization forms CP^+ in its electronic ground state of ^{2}E′ symmetry. The resulting photoelectron band exhibits a strong first-order splitting indicated by the large separation between the maxima of the twin band. The observed energy difference of ∼0.78 eV[27] between the maxima is explained as being due to JT distortion from the equilibrium geometry of CP.

Theoretical studies were carried out to understand the structural changes of CP resulting from the photoionization process.[28−32] Previous theoretical results agree that the first vertical ionization of CP occurs from a degenerate pair of in-plane e′ orbitals. The photoelectron spectrum was compared with the vertical ionization energies calculated using Koopman's theorem[33] and also by considering electron reorganization and correlation effects using a many-body Green's functions method.[30,34] The theoretical value of the vertical ionization potential of ∼10.7 eV obtained by von Niessen, Cederbaum, and Kraemer[34] using the Green's function method is in very good agreement with the experimental value of ∼10.6 eV. Bouma et al.[32] reported a value of ∼10.3 eV for the same quantity. Energy minimization studies have revealed that the photoionization from the E′ orbital of CP leads to species of C_{2v} symmetry; one is characterized by two long C−C bonds and one short C−C bond and the another one by two short and one long C−C bonds. The former corresponds to the $^2B_2$ and the latter to the $^2A_1$ component. With use of a MINDO/2 method, the JT stabilization energies of these two structures relative to a hypothetical D_{3h} cationic species were reported to be ∼9.5 and ∼9.2 kcal mol^{-1}, respectively.[28] JT splittings of ∼1.55 and ∼1.63 eV have been calculated for these two structures applying Koopman's theorem, which are twice as large as the experimentally observed splitting of ∼0.8 eV.[20]

CP is a nonlinear molecule and its 21 vibrational modes belong to the following symmetry species in the D_{3h} symmetry point group:

$$\Gamma_{\rm vib} = 3A_1' + A_2' + 4E' + A_1'' + 2A_2'' + 3E''$$

The symmetric direct product of either E′ or E″ representation yields

$$(E')^2 = (E'')^2 = A_1' + E'$$

This indicates that within the isolated E′/E″ electronic manifold only the single-prime vibrational modes play an important role in the nuclear dynamics. The totally symmetric vibrational modes of A_1' symmetry cannot lift the degeneracy of the E electronic manifold but can display Condon activity in the photoelectron band. On the other hand, the vibrational modes of E′ symmetry can lift the degeneracy of the E electronic manifold and can participate in the (E × e)−JT activity.

Although there were some activities on the theoretical side[28−32,34] to elucidate various stationary points on the potential energy surfaces of CP^+ and the vertical ionization energies as stated above, a rigorous dynamical study to unravel the vibrational structure of the photoelectron band is still missing. In the present article we set out to study the static and dynamic aspects of the JT coupling effects in the $\tilde{X}^2$E′ electronic manifold of CP^+. In this endeavor we devise a vibronic coupling scheme with the aid of an ab initio based quantum dynamical method. In our approach we first consider a linear vibronic coupling scheme and calculate the photoelectron band of the $\tilde{X}^2$E′ electronic manifold of CP^+. Despite some minor discrepancies in the detailed structure of the low-energy progression, the overall shape of the theoretical band obtained with this approach agrees very well with the experimental results. The bimodal shape of the photoelectron band is shown to be caused by the strong first-order JT coupling of the degenerate CH_2 wagging and ring deformation modes. We then extend this model by including the quadratic coupling terms in the Hamiltonian. The spectrum calculated with this latter approach has a similar overall shape to that obtained with the linear coupling approach. However, the low-energy progressions develop substructures and become somewhat irregular with the inclusion of the quadratic JT coupling terms.

The rest of the paper is organized in the following way. In section II we describe the vibronic coupling Hamiltonian and the computational details of the photoelectron spectrum. In section III ab initio calculations of the optimized geometry, harmonic vibrational frequencies, normal coordinates of CP, and the parameters of the Hamiltonian are discussed. In section IV the adiabatic potential energy surfaces of CP^+, their fit to the vibronic Hamiltonian of section II, and the static aspects of the problem are discussed. In this section we also show the theoretically calculated photoelectron band of the $\tilde{X}^2$E′ electronic manifold of CP^+ using a linear and a quadratic coupling scheme and compare it with the experimental result. Finally, summarizing remarks are presented in section V.

II. Theoretical Methods

A. The Vibronic Hamiltonian. The photoionization process of CP is described by a Franck−Condon (FC) transition from its electronic ground state to the $\tilde{X}^2$E′ electronic manifold of CP^+. Ionization of an electron from the 3e′ valence molecular orbital of CP generates CP^+ in its $\tilde{X}^2$E′ ground electronic state. A distortion along any of the E′ vibrational modes splits the electronic degeneracy of CP^+.

To monitor the nuclear motion in this degenerate electronic manifold, we construct a model vibronic Hamiltonian[7] in the dimensionless normal coordinates pertinent to the D_{3h} symmetry point group of the ground electronic state of CP. The vibrational motion in this initial electronic state is treated as harmonic. We resort to a diabatic[35] electronic representation in which the diverging kinetic coupling terms of the adiabatic electronic representation change into smooth potential couplings. Rather than constructing it explicity by solving the differential equation for the adiabatic-to-diabatic mixing angle,[36] we assume it to be given by the electronic wave functions of the D_{3h} reference geometry. In such a representation the elements of the vibronic Hamiltonian are smooth functions of the nuclear coordinates and the Condon approximation holds well in the photoionization process.[37] In what follows, we define Q_i as the dimensionless normal coordinate (a more explicit definition follows in the next section) of CP associated with the vibrational mode ν_i. The vibrational modes $i = 1-3$ are of A_1' symmetry (Condon active) and $i = 4-7$ are of E′ symmetry (JT active). The nature of these modes is described in section IV. The diabatic vibronic Hamiltonian for the ionization of an electron from the 3e′ orbital of CP can be expressed as

$$\mathscr{H} = \mathscr{H}_0\mathbf{1} + \Delta\mathscr{H} \tag{1}$$

Here, $\mathscr{H}_0 = \mathscr{T}_N + \mathscr{V}_0$, with

$$\mathscr{T}_N = -\frac{1}{2}\sum_{i=1}^{3}\omega_i\left(\frac{\partial^2}{\partial {Q_i}^2}\right) - \frac{1}{2}\sum_{i=4}^{7}\omega_i\left[\frac{\partial^2}{\partial {Q_{xi}}^2} + \frac{\partial^2}{\partial {Q_{yi}}^2}\right] \tag{2}$$

$$\mathscr{V}_0 = \frac{1}{2}\sum_{i=1}^{3}\omega_i {Q_i}^2 + \frac{1}{2}\sum_{i=4}^{7}\omega_i({Q_{xi}}^2 + {Q_{yi}}^2) \tag{3}$$

is the Hamiltonian matrix associated with the electronic ground state of CP and is defined in terms of unperturbed harmonic oscillators with frequencies ω_i. $\mathbf{1}$ is a (2 × 2) unit matrix. $\Delta\mathscr{H}$ describes the change in electronic energy upon ionization. This is a nondiagonal (2 × 2) matrix and its elements represent the interacting (component) diabatic electronic states of CP$^+$ which are expanded in a Taylor series up to second order (neglecting the terms due to double-prime vibrational modes) about the reference D_{3h} equilibrium geometry of CP in conjunction with the elementary symmetry selection rules[7,37] (cf. section I). Various contributions to $\Delta\mathscr{H}$ are described in the following way

$$\Delta\mathscr{H} = \Delta\mathscr{H}^0 + \Delta\mathscr{H}^{\mathrm{ls}} + \Delta\mathscr{H}^{\mathrm{lJT}} + \Delta\mathscr{H}^{\mathrm{qs}} + \Delta\mathscr{H}^{\mathrm{qJT}} + \Delta\mathscr{H}^{\mathrm{bl}} \tag{4}$$

with

$$\Delta\mathscr{H}^0 = \begin{pmatrix} E^0_{\mathrm{E}'} & 0 \\ 0 & E^0_{\mathrm{E}'} \end{pmatrix} \tag{5}$$

1. Linear Coupling. Coupling by the symmetric (A_1') modes

$$\Delta\mathscr{H}^{\mathrm{ls}} = \begin{pmatrix} \sum_{i=1}^{3}\kappa_i Q_i & 0 \\ 0 & \sum_{i=1}^{3}\kappa_i Q_i \end{pmatrix} \tag{6}$$

Coupling by the JT (E′) modes,

$$\Delta\mathscr{H}^{\mathrm{lJT}} = \begin{pmatrix} \sum_{i=4}^{7}\lambda_i Q_{xi} & \sum_{i=4}^{7}\lambda_i Q_{yi} \\ \sum_{i=4}^{7}\lambda_i Q_{yi} & -\sum_{i=4}^{7}\lambda_i Q_{xi} \end{pmatrix} \tag{7}$$

2. Quadratic Coupling. Coupling by the symmetric (A_1') modes,

$$\Delta\mathscr{H}^{\mathrm{qs}} = \begin{pmatrix} \frac{1}{2}\sum_{i=1}^{3}\gamma_i {Q_i}^2 & 0 \\ 0 & \frac{1}{2}\sum_{i=1}^{3}\gamma_i {Q_i}^2 \end{pmatrix} \tag{8}$$

Coupling by the JT (E′) modes,

$$\Delta\mathscr{H}^{qJT} = \begin{pmatrix} \frac{1}{2}\sum_{i=4}^{7}(\gamma_i({Q_{xi}}^2 + {Q_{yi}}^2) + \eta_i({Q_{xi}}^2 - {Q_{yi}}^2)) & -\sum_{i=4}^{7}\eta_i Q_{xi}Q_{yi} \\ -\sum_{i=4}^{7}\eta_i Q_{xi}Q_{yi} & \frac{1}{2}\sum_{i=4}^{7}(\gamma_i({Q_{xi}}^2 + {Q_{yi}}^2) - \eta_i({Q_{xi}}^2 - {Q_{yi}}^2)) \end{pmatrix} \tag{9}$$

3. Bilinear Coupling. Coupling by the E′−E′ and A_1'−E′ modes,

$$\Delta\mathscr{H}^{\mathrm{bl}} = \begin{pmatrix} \begin{array}{l} \frac{1}{2}(\sum_{i,j=4,i\neq j}^{7}\gamma'_{ij}(Q_{xi}Q_{xj} + Q_{yi}Q_{yj}) \\ \quad + \eta'_{ij}(Q_{xi}Q_{xj} - Q_{yi}Q_{yj})) \\ \quad + \frac{1}{2}\sum_{i=1}^{3}\sum_{j=4}^{7}\gamma''_{ij}Q_iQ_{xj} \end{array} & \begin{array}{l} \frac{1}{2}\sum_{i,j=4,i\neq j}^{7}\eta''_{ij}(Q_{yi}Q_{xj} + Q_{yj}Q_{xi}) \\ \quad + \frac{1}{2}\sum_{i=1}^{3}\sum_{j=4}^{7}\gamma''_{ij}Q_iQ_{yj} \end{array} \\ \begin{array}{l} \frac{1}{2}\sum_{i,j=4,i\neq j}^{7}\eta''_{ij}(Q_{yi}Q_{xj} + Q_{yj}Q_{xi}) \\ \quad + \frac{1}{2}\sum_{i=1}^{3}\sum_{j=4}^{7}\gamma''_{ij}Q_iQ_{yj} \end{array} & \begin{array}{l} \frac{1}{2}(\sum_{i,j=4\ i\mp j}^{7}\gamma'_{ij}(Q_{xi}Q_{xj} + Q_{yi}Q_{yj}) \\ \quad -\eta'_{ij}(Q_{xi}Q_{xj} - Q_{yi}Q_{yj})) \\ \quad - \frac{1}{2}\sum_{i=1}^{3}\sum_{j=4}^{7}\gamma''_{ij}Q_iQ_{xj} \end{array} \end{pmatrix} \tag{10}$$

The parameters in the above equations have the following identities. The vertical ionization energy of the $\tilde{\mathrm{X}}^2\mathrm{E}'$ electronic state of CP$^+$ is defined as $E^0_{\mathrm{E}'}$. The linear intrastate coupling constants for the totally symmetric vibrational modes are given by κ_i, whereas λ_i denote the linear JT coupling constants for the degenerate vibrational modes. The quantity γ_i represents the diagonal second-order coupling parameter for the mode i and η_i represents the quadratic JT coupling parameter. The bilinear JT coupling (E′−E′) parameters are given by γ'_{ij}, η'_{ij}, and η''_{ij} and the symmetric−JT ($A_1'-E'$) coupling parameters are given by γ_{ij}''. The x and y components of the degenerate vibrational modes $\nu_4-\nu_7$ are denoted by Q_{xi} and Q_{yi}, respectively. It can be seen that in the absence of the bilinear coupling terms (eq 10) the (E × e)−Hamiltonian matrix (eqs 5−9) acquires a very simple structure, and the totally symmetric modes are separable from the JT modes. Therefore, they can be treated separately in the nuclear dynamical simulation.

B. Photoelectron Spectrum. The photoelectron spectrum for a transition to the $\tilde{\mathrm{X}}^2\mathrm{E}'$ electronic manifold of CP is described by Fermi's Golden rule. The photoelectron intensity is given by

$$P(E) = \sum_{v}|\langle\Psi_v|\hat{T}|\Psi_0\rangle|^2\,\delta(E - E_v + E_0) \tag{11}$$

where $|\Psi_0\rangle$ is the initial vibrational and electronic ground state of CP with energy E_0. $|\Psi_{\mathrm{v}}\rangle$ is the final $\tilde{\mathrm{X}}^2\mathrm{E}'$ vibronic state of CP$^+$ and E_{v} is the corresponding vibronic energy. $\hat{T}$ is the transition operator that describes the interaction of the valence 3e′ electron of CP with the external radiation with energy E. In the present study, the initial and the final states can be expressed as follows:

$$|\Psi_0\rangle = |\Phi^0\rangle|\chi_0^0\rangle \tag{12}$$

$$|\Psi_{\mathrm{v}}\rangle = |\Phi^{E_x}\rangle|\chi_{\mathrm{v}}^{E_x}\rangle + |\Phi^{E_y}\rangle|\chi_{\mathrm{v}}^{E_y}\rangle \tag{13}$$

where $|\Phi\rangle$ and $|\chi\rangle$ represent the diabatic electronic and vibrational part of the wave function, respectively. The superscripts 0 and E_x/E_y refer to the $^1\mathrm{A}_1'$ electronic ground state of CP and x/y components of the $\tilde{\mathrm{X}}^2\mathrm{E}'$ electronic state of CP$^+$, respectively. Using eqs 12 and 13, the excitation function of eq 11 can be rewritten as

$$P(E) = \sum_{v}|\tau^{E_x}\langle\chi_{\mathrm{v}}^{E_x}|\chi_0^0\rangle + \tau^{E_y}\langle\chi_{\mathrm{v}}^{E_y}|\chi_0^0\rangle|^2\delta(E - E_{\mathrm{v}} + E_0) \tag{14}$$

TABLE 1: Equilibrium Geometry of CP in Its Ground Electronic State ($^1A_1'$) along with the Experimental Results of ref 45

	∠H−C−H (deg)	∠C−C−C (deg)	C−H (Å)	C−C (Å)
MP2/cc-pVTZ	115.08	60	1.078	1.503
expt[45]	117.08	59.98	1.074	1.499

where

$$\tau^m = \langle \Phi^m | \hat{T} | \Phi^0 \rangle \tag{15}$$

denote the generalized oscillator strengths of the final $\tilde{X}^2E'$ electronic manifold of CP$^+$. In rewriting eq 14, the matrix elements of the transition operator are considered to be weakly varying functions of nuclear coordinates and are treated as constants, in accordance with the applicability of the generalized Condon approximation in the diabatic electronic basis.[37] To calculate the photoelectron spectrum, we solve the eigenvalue equation

$$\mathcal{H} | \Psi_v \rangle = E_v | \Psi_v \rangle \tag{16}$$

numerically, by representing the vibronic Hamiltonian $\mathcal{H}$ in a direct product basis of harmonic oscillator eigenstates of $\mathcal{H}_0$. In this basis $|\chi_v^m\rangle$ takes the following form:[7]

$$|\chi_v^m\rangle = \sum_{n_1, n_2, \ldots, n_k} a^m_{v, n_1, n_2, \ldots, n_k} |n_1\rangle |n_2\rangle \ldots |n_k\rangle \tag{17}$$

Here m is the electronic state index, n_l is the quantum number associated with the lth vibrational mode, and k is the total number of such modes. The summation runs over all possible combinations of quantum numbers associated with each mode. For each vibrational mode the oscillator basis is suitably truncated in the numerical calculations. The maximum level of excitation for each mode can be approximately estimated from its excitation strength. This number is further confirmed from the convergence behavior of the spectral envelope. The Hamiltonian matrix expressed in a direct product Harmonic oscillator basis is highly sparse. We tri-diagonalize this sparse Hamiltonian matrix by the Lanczos algorithm[39] prior to diagonalization. The diagonal elements of the resulting eigenvalue matrix give the position of the vibronic lines and the relative intensities are obtained from the squared first components of the Lanczos eigenvectors.[38,40]

III. Ab Initio Calculations

A. Optimized Geometry, Harmonic Vibrational Frequencies, and Normal Coordinates of Cyclopropane in the Ground Electronic State. The geometry optimization and the calculation of harmonic vibrational frequencies of cyclopropane in its ground electronic state ($^1A_1'$) are carried out at the Møller−Plesset perturbation theory (MP2) level employing the correlation−consistent polarized valence triple−ζ (cc-pVTZ) Gaussian basis set of Dunning.[41] The electronic structure calculations were performed using the Gaussian program package.[44] The optimized geometry parameters of CP in its ($^1A_1'$) electronic state are documented in Table 1 along with the available experimental results.[45] It can be seen from Table 1 that MP2 equilibrium geometry parameters correspond well with the corresponding experimental values, except the ∠H−C−H angle, which is ∼2° smaller than the experimental value. The MP2/cc-pVTZ value of the vertical ionization energy $E^0_{E'}$ is 10.8008 eV.

TABLE 2: Coupling Constants for the $\tilde{X}^2E'$ Electronic Manifold of the Cyclopropane Radical Cation ($C_3H_6^+$) Derived from the OVGF Data and the Harmonic Vibrational Frequencies of Cyclopropane in Its Electronic Ground ($\tilde{X}^1A_1'$) State[a]

modes (symmetry)	κ or λ $\tilde{X}^2E'$	γ $\tilde{X}^2E'$	η $\tilde{X}^2E'$	ω_i MP2/cc-pVTZ	ω_i expt[47]
$\nu_1(A_1')$	−0.1091	-9.5098×10^{-4}		0.1531	0.1473
$\nu_2(A_1')$	0.2144	2.1751×10^{-3}		0.1902	0.1829
$\nu_3(A_1')$	0.0176	6.620×10^{-4}		0.3965	0.3744
$\nu_4(E_1')$	0.3201	1.4419×10^{-3}	-1.886×10^{-3}	0.1129	0.1074
$\nu_5(E_1')$	0.3701	5.784×10^{-3}	-3.7048×10^{-3}	0.1309	0.1270
$\nu_6(E_1')$	0.0692	-6.5864×10^{-3}	-1.824×10^{-3}	0.1841	0.1778
$\nu_7(E_1')$	0.0328	2.4408×10^{-3}	3.3461×10^{-4}	0.3954	0.3743

[a] All quantities are in eV if not otherwise stated. The experimental results represent the fundamental vibrational frequencies.

The ab initio force constant matrix for the ground electronic state of CP is obtained with the cc-pVTZ basis set at the MP2 level. On diagonalization of this force constant matrix, the harmonic vibrational frequencies (ω_i) are obtained. The present theoretical vibrational frequencies along with the experimental ones are collected in the last two columns of Table 2. The apparent deviations between the two can be attributed to the fact that the experimental results represent the fundamental vibrational frequencies.

Along with the harmonic vibrational frequencies the transformation matrix from the symmetry coordinates to the mass-weighted normal coordinates is obtained. The dimensionless normal coordinates (Q_i) are then obtained by multiplying the latter with $\sqrt{\omega_i}$.

B. Coupling Parameters of the Hamiltonian. The coupling parameters of the Hamiltonian (eqs 6−10) represent the derivatives of the adiabatic potentials of CP$^+$ of appropriate order with respect to the dimensionless normal coordinates, calculated at the equilibrium geometry of CP (**Q=0**).[46] The linear intrastate (κ_i) and the JT (λ_i) coupling parameters are defined as follows,

$$\kappa_i = \left(\frac{\partial V_E}{\partial Q_i} \right) \Bigg|_{\mathbf{Q=0}}, \qquad i = 1-3 \tag{18}$$

$$\lambda_i = \frac{1}{2} \left(\frac{\partial \Delta V_E}{\partial Q_i} \right) \Bigg|_{\mathbf{Q=0}}, \qquad i = 4-7 \tag{19}$$

where V_E denotes the adiabatic potential energy of the degenerate $\tilde{X}^2E'$ electronic state of CP$^+$. The quantity ΔE is the (signed) difference of the JT split potential energy surfaces of the $\tilde{X}^2E'$ electronic state. The diagonal second-order coupling parameters γ_i for both symmetric and degenerate vibrational modes are obtained from the following expressions,

$$\gamma_i = \left(\frac{\partial^2 V_E}{\partial {Q_i}^2} \right) \Bigg|_{\mathbf{Q=0}}, \qquad i = 1-3 \tag{20}$$

$$\gamma_i = \left(\frac{\partial^2 \bar{V}_E}{\partial {Q_i}^2} \right) \Bigg|_{\mathbf{Q=0}}, \qquad i = 4-7 \tag{21}$$

where $\bar{V}_E$ is the mean of the JT split potential energy surfaces of the $\tilde{X}^2E'$ electronic state of CP$^+$.

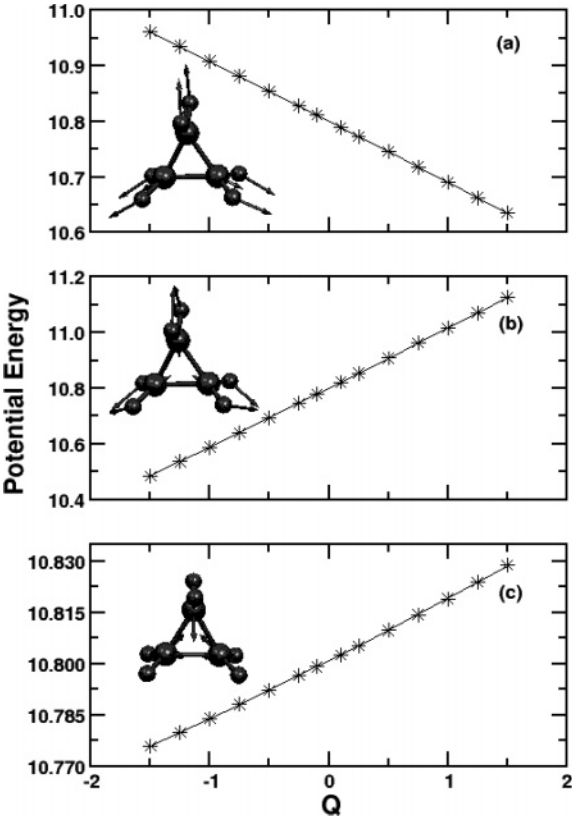

Figure 1. Vertical ionization potential of CP pertinent to the first photoelectron band, plotted along the dimensionless normal coordinates of the symmetric vibrational modes ν_1 (panel a), ν_2 (panel b), and ν_3 (panel c). The OVGF energy values are shown by the asterisks and a quadratic fit to these points is shown by the solid lines. The linear and the diagonal quadratic coupling parameters listed in Table 2 are obtained from the above fits.

The quadratic (η_i) coupling parameters are calculated from the (signed) difference of the JT splitted potential energy surfaces:

$$\eta_i = \frac{1}{2}\left(\frac{\partial^2 \Delta E}{\partial {Q_i}^2}\right)\Bigg|_{\mathbf{Q=0}}, \qquad i = 4-7 \tag{22}$$

The bilinear E′−E′ and A_1'−E′ coupling parameters are evaluated in a similar way either from the mean or from the (signed) difference of the JT splitted potential energy surfaces by suitably displacing CP^+ along two normal modes of vibration simultaneously.

To estimate these coupling parameters, we performed direct calculations of vertical ionization energies of CP by the outer-valence Green's function (OVGF) method[42,43] employing the cc-pVTZ basis set. The electronic structure calculations are carried out as a function of the dimensionless normal mode displacement (from $\mathbf{Q}=\mathbf{0}$) coordinates and for Q_i ($i = 1-7$) $=$ -1.5 (0.25) 1.5, using the Gaussian program package.[44] The vertical ionization energies thus obtained are equated with the adiabatic potential energy difference of the $\tilde{X}^2E'$ electronic state of CP^+ and $\tilde{X}^1A_1'$ electronic state of CP along the respective normal modes of vibration. These energies are then fitted to the adiabatic form of the diabatic Hamiltonian described in eqs 6−10 by a least-squares procedure and thereby the coupling parameters are derived.

In Figure 1a−c the adiabatic potential energy values of $\tilde{X}^2E'$ electronic state of CP^+ measured relative to the $\tilde{X}^1A_1'$ electronic state of CP (these are the vertical ionization energy values obtained from the OVGF calculations) along the dimensionless normal coordinate of the tuning[7] (A_1') vibrational modes ν_1, ν_2, and ν_3 are plotted. The asterisks in each panel represent the computed data and a quadratic (excluding the bilinear coupling) fit to these data is shown by the solid line. The nature of each of these vibrations is included in the respective panel by an insert. The vibrational modes ν_1, ν_2, and ν_3 represent C−C stretching, CH_2 scissoring, and symmetric C−H stretching motion, respectively.[47] It can be seen that the degeneracy of the $\tilde{X}^2E'$ electronic state of CP^+ is not lifted when displacing along these vibrations. The linear (κ_i) and the second-order (γ_i) coupling parameters for these modes resulting from the above fits are included in Table 2.

The mean of the JT splitted potential energy surfaces when distorting along the *x* component of the degenerate vibrational modes ν_4, ν_5, ν_6, and ν_7 is plotted in Figure 2a−d, respectively, as a function of their dimensionless normal coordinates. The nature of these vibrations is also schematically shown in the respective panel as an insert. They represent CH_2 wagging, ring deformation, CH_2 scissoring, and asymmetric C−H stretching motion, respectively, in that order.[47] The computed points in each panel are shown by the asterisks and a fit to these points is shown by the solid line. It can be seen, from eqs 6−9 that, in absence of the bilinear coupling, the above fits yield the diagonal second-order coupling parameter γ_i for the *i*th vibrational mode. The value of these parameters obtained from the above fits are included in Table 2.

The linear and quadratic JT coupling parameters for the degenerate vibrational modes ν_4−ν_7 are evaluated by fitting the (signed) difference of the JT split potential energy surfaces along these modes. In Figure 3a−d this energy difference is plotted along the dimensionless normal coordinates of the *x* component of the respective mode. The asterisks in each panel denote the computed energies and the solid line superimposed on them represents the quadratic fit (excluding bilinear coupling terms). The value of the linear (λ_i) and quadratic (η_i) JT parameters thus obtained from the above fits are included in Table 2.

IV. Results and Discussion

A. Adiabatic Potential Energy Surfaces. On diagonalization of the diabatic electronic Hamiltonian matrix of eqs 5−9, the adiabatic potential energy surfaces are obtained.[7] First, we consider the electronic Hamiltonian matrix within the linear vibronic coupling scheme only (i.e., excluding the contributions from eqs 8−10). The adiabatic potential energy surfaces of this linear vibronic Hamiltonian are given by its eigenvalues[7]

$$\mathscr{V}_{\mp}(Q) = \mathscr{V}_0(Q) + E^0_{E'} + \sum_{i=1}^{3}\kappa_i Q_i \mp \sqrt{\left(\sum_{i=4}^{7}\lambda_i Q_{xi}\right)^2 + \left(\sum_{i=4}^{7}\lambda_i Q_{yi}\right)^2} \tag{23}$$

where $\mathscr{V}_-$ and $\mathscr{V}_+$ refer to the lower and upper adiabatic sheets of the $\tilde{X}^2E'$ electronic manifold of CP^+, respectively. The quantity $\mathscr{V}_0(Q)$ is given by eq 3. The analytic form of the argument of the square root in eq 23 represents a cusp in the vicinity of the JT undistorted configuration at $\mathbf{Q}=\mathbf{0}$.

The topographical features of the (E × e)−JT Hamiltonian are well-known in the literature.[2,7,9−13,15−17] We only briefly discuss them here with reference to cyclopropane. The cuts of the adiabatic potential energy surfaces described by eq 23 along the normal coordinates of the vibrational modes ν_1−ν_7 are shown in Figure 4a−c for the tuning (A_1') modes and in Figure 5a−d for the coupling (E′) modes. The three totally symmetric

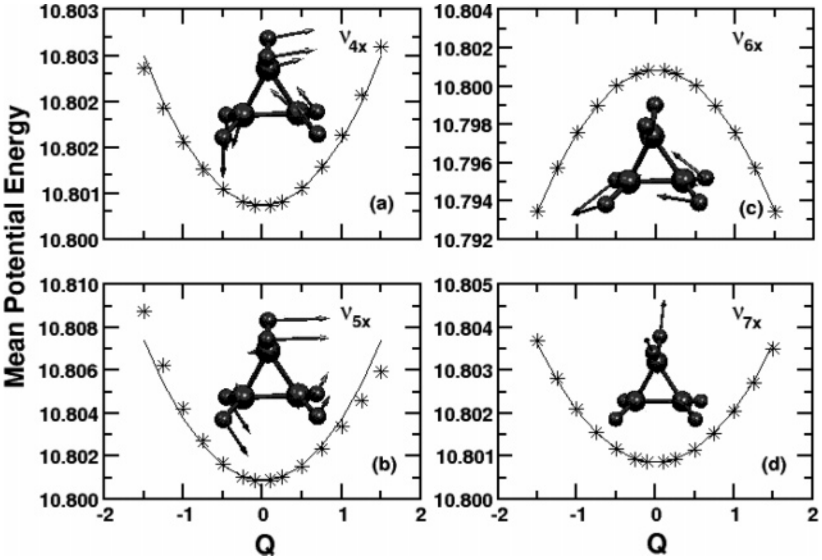

Figure 2. Mean potential energy of the JT split adiabatic sheets of the $\tilde{X}^2E'$ electronic manifold of CP$^+$ plotted along the dimensionless normal coordinates of the *x* components of the degenerate vibrational modes ν_4, ν_5, ν_6, and ν_7 in panels a, b, c, and d, respectively. The OVGF data are shown by the asterisks and a parabolic fit to these data is shown by the solid lines. The diagonal quadratic coupling constants for the JT modes listed in Table 2 are derived from the above fits.

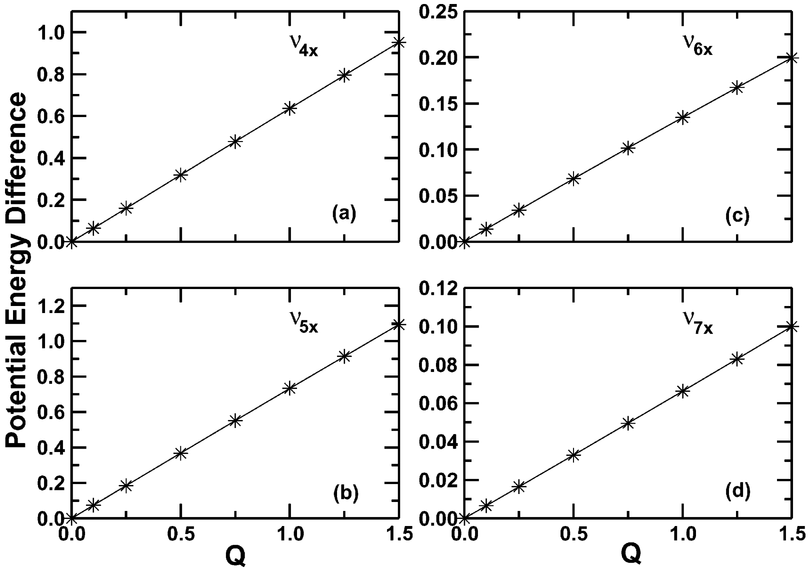

Figure 3. Potential energy difference of the JT split adiabatic sheets of the $\tilde{X}^2E'$ electronic manifold of CP$^+$ plotted along the dimensionless normal coordinates of the *x* components of the degenerate vibrational modes ν_4, ν_5, ν_6, and ν_7 in panels a, b, c, and d, respectively. The OVGF data are shown by the asterisks and a quadratic fit to these data is shown by the solid line. The linear and the quadratic JT coupling parameters listed in Table 2 are derived from the above fits.

modes $\nu_1-\nu_3$ cannot lift the degeneracy of the $\tilde{X}^2E'$ electronic state of CP$^+$. However, depending on their coupling strength, they can shift the potential energy minimum of the ionic state considerably away from the equilibrium geometry of the neutral and display tuning activities in the photoelectron spectrum. These modes, in fact, tune the vertical ionization energies of the ionic states. The mode ν_1 represents the C$-$C stretching vibration. The potential energy of the $\tilde{X}^2E'$ state as a function of its normal coordinate Q_1 is shown in Figure 4a. The excitation strength, defined as $(\kappa^2/2\omega^2)$,[7] of this mode is included in the panel. Since it has small excitation strength, it shifts the potential energy minimum of the $\tilde{X}^2E'$ state of CP$^+$ only slightly relative to the ground state of CP at $\mathbf{Q}=\mathbf{0}$. The vibrational mode ν_2 represents the CH$_2$ scissoring motion. The potential energy of the $\tilde{X}^2E'$ state of CP$^+$ along the normal coordinate Q_2 is shown in Figure 4b. The excitation strength of this mode is about 2.5 times higher than that of ν_1 and, as a result, it shifts the potential minimum of the ionic state to a larger value of Q_2. The vibrational mode ν_3 represents the symmetric C$-$H stretching motion. It can be seen from Figure 4c that this mode has extremely small coupling strength ($\sim$0.0009) and the potential minimum of the $\tilde{X}^2E'$ state of CP$^+$ essentially remains at the ground-state equilibrium position when distorting along this vibrational mode. One may practically disregard this high-frequency mode in the dynamical simulations.

The potential energy surfaces of the $\tilde{X}^2E'$ manifold of CP$^+$ along the normal coordinate of the *x* component of the degenerate vibrational modes $\nu_4-\nu_7$ are shown in Figure 5a$-$d. The degeneracy of the $\tilde{X}^2E'$ electronic manifold is destroyed when distorting along these vibrational modes. The extent of splitting of the degeneracy depends on their coupling strength, given in each panel. It can be seen that the vibrational modes ν_4 (CH$_2$ wagging) and ν_5 (ring deformation) have large first-order coupling (cf. Table 2) and cause considerable splitting of

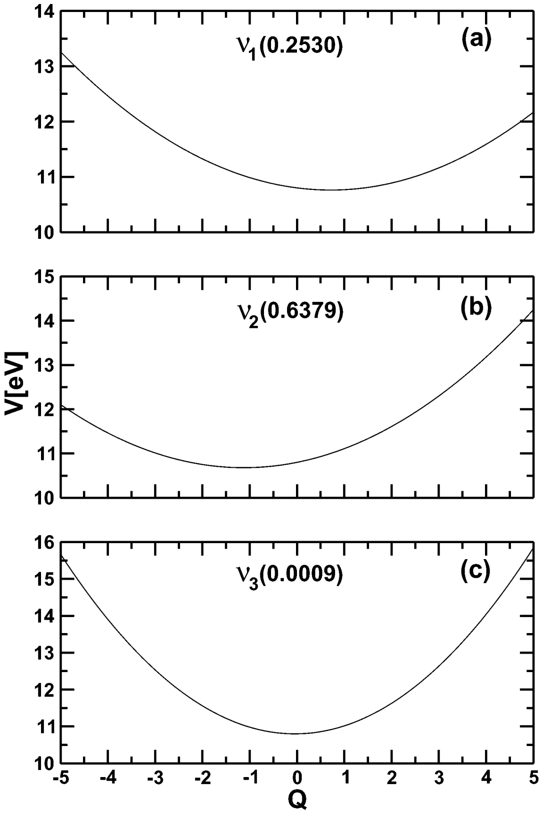

Figure 4. Adiabatic potential energy of the $\tilde{X}^2E'$ electronic manifold of CP^+ as a function of the dimensionless normal coordinates of the symmetric (A'_1) vibrational modes ν_1 (panel a), ν_2 (panel b), and ν_3 (panel c). The potential energy surfaces are obtained with the linear vibronic coupling scheme. The number in the parentheses indicate the excitation strength, $\kappa^2/2\omega^2$, of the respective mode. The equilibrium geometry of CP in its electronic ground state ($^1A'_1$) corresponds to $\mathbf{Q}=\mathbf{0}$.

the degeneracy. These two modes are expected to be significantly excited in the photoelectron transition. On the other hand, the weak splitting of the degeneracy caused by the vibrational modes ν_6 (CH_2 scissoring) and ν_7 (asymmetric C−H stretching) may not have any significant impact on the photoelectron transition.

The two sheets of the $\tilde{X}^2E'$ electronic manifold remain degenerate (eq 23) in absence of any JT distortion, that is, Q_i ($i = 4-7$) $= 0$. These two sheets form conical intersections and the minimum of this intersection seam occurs at Q_i^0 ($i = 1-3$) $= -\kappa_i/\omega_i$, in the space of A'_1 vibrational modes with an energy[7]

$$\mathscr{V}_{\rm min}^{(c)} = E_{E'}^0 - \frac{1}{2}\sum_{i=1}^{3}\frac{\kappa_i^{\,2}}{\omega_i} \tag{24}$$

This global minimum on $\mathscr{V}_-$ at the D_{3h} equilibrium geometry becomes a cusp when distorted along any of the two components of the degenerate vibrational modes. The minimum of $\mathscr{V}_+$ remains at the minimum of the seam of conical intersections and new minima appear on $\mathscr{V}_-$ at Q_i^0 ($i = 1-3$) $= -\kappa_i/\omega_i$ and Q_{pi}^0 ($p = x/y$, $i = 4-7$) $= \pm\lambda_{pi}/\omega_{pi}$ with an energy

$$\mathscr{V}_-^0 = E_{E'}^0 - \frac{1}{2}\sum_{i=1}^{3}\frac{\kappa_i^{\,2}}{\omega_i} - \frac{1}{2}\sum_{i=4}^{7}\frac{\lambda_{pi}^{\,2}}{\omega_{pi}} \tag{25}$$

In multidimensional space this results in a Mexican hat topography of the JT split potential energy surfaces. The JT stabilization energy amounts to

$$\sum_{i=4}^{7}\lambda_{pi}^{\,2}/2\omega_{pi}$$

Considering the data collected in Table 2, one can see that the $\mathscr{V}_{\rm min}^{(c)} = 10.6408$ eV, occurs at $Q_1^0 = 0.7126$, $Q_2^0 = -1.1272$, and $Q_3^0 = -0.444$. The new minima on $\mathscr{V}_-^0$ (eq 25) for the JT distorted geometry occurs at $Q_{4x}^0 = 2.8351$, $Q_{5x}^0 = 2.827$, $Q_{6x}^0 = 0.3759$, and $Q_{7x}^0 = 0.0829$ with an energy $\mathscr{V}_-^0 = 9.6495$ eV. The JT stabilization energy amounts to ∼0.9913 eV.

The above stationary points of the potential energy surfaces are further modified when the quadratic coupling terms in the Hamiltonian (eqs 8 and 9) are considered. In absence of any bilinear coupling (eqs 5−9) the adiabatic potential energy surfaces (eq 23) are modified as

$$\begin{aligned}\mathscr{V}_\mp(Q) = \mathscr{V}_0(Q) + E_{E'}^0 + \sum_{i=1}^{3}\kappa_iQ_i + \frac{1}{2}\sum_{i=1}^{3}\gamma_iQ_i^{\,2} + {}\\ \frac{1}{2}\sum_{i=4}^{7}\gamma_i(Q_{xi}^{\,2} + Q_{yi}^{\,2}) \mp {}\\ \sqrt{\left[\sum_{i=4}^{7}\left(\lambda_iQ_{xi} + \frac{1}{2}\eta_i(Q_{xi}^{\,2} - Q_{yi}^{\,2})\right)\right]^2 + \left[\sum_{i=4}^{7}(\lambda_iQ_{yi} - \eta_iQ_{xi}Q_{yi})\right]^2}\end{aligned} \tag{26}$$

In the space of A'_1 vibrational modes the minimum of the seam of conical intersections now occurs at $Q_i^0(i = 1-3) = -\kappa_i/(\omega_i + \gamma_i)$, and the energy at the minimum is given by

$$\mathscr{V}_{\rm min}^{(c)} = E_{E'}^0 - \frac{1}{2}\sum_{i=1}^{3}\frac{\kappa_i^{\,2}}{(\omega_i + \gamma_i)} \tag{27}$$

Along the degenerate modes, two solutions, $Q_{xi} = \mp\lambda_i/(\omega_i + \gamma_i \pm \eta_i)$ ($i = 4-7$), are obtained with energies

$$\mathscr{V}_-^0 = E_{E'}^0 - \frac{1}{2}\sum_{i=1}^{3}\frac{\kappa_i^{\,2}}{(\omega_i + \gamma_i)} - \frac{1}{2}\sum_{i=4}^{7}\frac{\lambda_i^{\,2}}{(\omega_i + \gamma_i + \eta_i)} \tag{28}$$

and

$$\mathscr{V}_-^{\rm sp} = E_{E'}^0 - \frac{1}{2}\sum_{i=1}^{3}\frac{\kappa_i^{\,2}}{(\omega_i + \gamma_i)} - \frac{1}{2}\sum_{i=4}^{7}\frac{\lambda_i^{\,2}}{(\omega_i + \gamma_i - \eta_i)} \tag{29}$$

where $\mathscr{V}_-^0$ and $\mathscr{V}_-^{\rm sp}$ refer to the energy of the minimum and the saddle point, respectively, for the signs of the coupling constants as given in Table 2. With the data listed in Table 2 one obtains $\mathscr{V}_{\rm min}^{(c)} = 10.6419$ eV at $Q_1^0 = 0.7171$, $Q_2^0 = -1.1145$, and $Q_3^0 = -0.0443$. The new minima on $\mathscr{V}_-$ for the JT distorted geometry occur at $Q_{4x}^0 = 2.7541$, $Q_{5x}^0 = 2.6363$, $Q_{6x}^0 = 0.3859$, and $Q_{7x}^0 = 0.0825$, with energy $\mathscr{V}_-^0 = 9.6563$ eV. The saddle point occurs at $Q_{4x}^{\rm sp} = -2.8464$, $Q_{5x}^{\rm sp} = -2.7831$, $Q_{6x}^{\rm sp} = -0.3939$, and $Q_{7x}^{\rm sp} = -0.0824$, with energy $\mathscr{V}_-^{\rm sp} = 9.6985$ eV. The JT stabilization energy amounts to ∼0.9856 eV. A comparison with the linear coupling results (discussed above) reveals that when the quadratic couplings are considered, both $\mathscr{V}_{\rm min}^{(c)}$ and $\mathscr{V}_-^0$ shift to slightly higher energy values. The shift in the value of $\mathscr{V}_-^0$ is

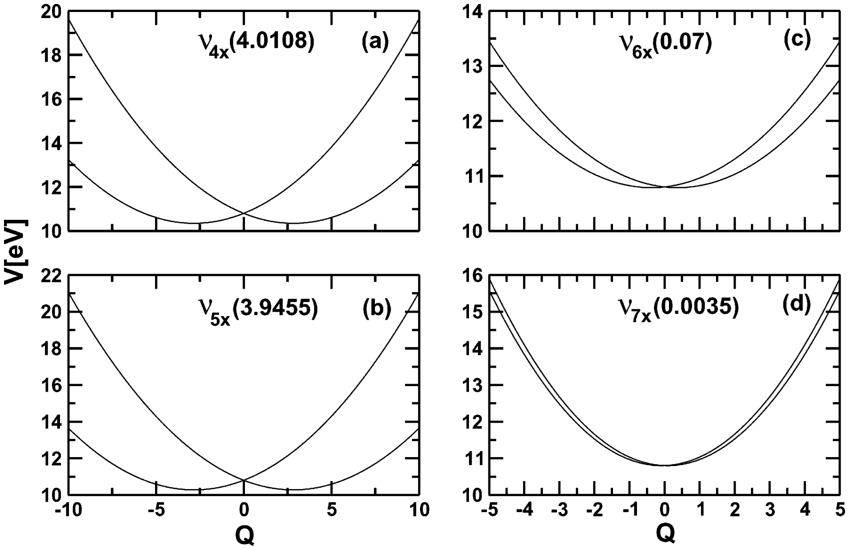

Figure 5. Same as in Figure 4, plotted as a function of the *x* component of the dimensionless normal coordinates of the degenerate (E′) vibrational modes: (a) ν_{4x}, (b) ν_{5x}, (c) ν_{6x}, and (d) ν_{7x}.

relatively greater than that in $\mathscr{V}^{(c)}_{\text{min}}$. As a result, the JT stabilization energy also decreases.

B. Photoelectron Spectrum. In this section we report on the photoelectron band of the $\tilde{X}^2E'$ electronic manifold of CP$^+$, calculated by employing the Hamiltonian of eqs 5−9 and the parameters of Table 2. The theoretical results are compared with the earlier[20−23] and most recent experimental results.[27] The experimental photoelectron band revealed a characteristic bimodal structure indicating a strong first-order JT splitting in the $\tilde{X}^2E'$ electronic manifold of CP$^+$. The energetic separation between the two maxima in the bimodal profile is reported to be ∼0.78 eV,[27] which amounts to this JT splitting. A fairly resolved vibrational progression is observed in the low-energy wing of the bimodal spectral envelope, which becomes extremely diffuse with increasing energy. An average spacing of 60 meV is reported for the resolved structure at low energies, which is mainly attributed to the progression of the degenerate vibrational mode ν_4.[27]

We in the following discuss this $\tilde{X}^2E'$ photoelectron band calculated with the linear as well as the quadratic vibronic coupling scheme as illustrated above. We again note that in the absence of the bilinear coupling terms, the Hamiltonian is decoupled in terms of the symmetric (A_1') and degenerate (E′) vibrational modes. We utilize this property of the Hamiltonian in our numerical calculations and calculate two partial spectra by considering the totally symmetric and degenerate vibrational modes separately in the nuclear dynamics. Finally, these two partial spectra are convoluted to generate the complete spectrum. This substantially reduces the effective dimensionality of the secular matrix in each calculation. Furthermore, we did not consider the degenerate vibrational mode ν_7 in the dynamics, as it has very low coupling strength and causes only negligible splitting in the $\tilde{X}^2E'$ electronic manifold (cf. Figure 5d).

In Figure 6a the spectrum obtained with three totally symmetric modes ν_1, ν_2, and ν_3 within the linear vibronic coupling scheme is shown. The spectral intensity in arbitrary units is plotted as a function of the energy of the final vibronic state E. For the symmetric modes all nuclear motions decouple and the spectrum is obtained by convoluting the spectra of the individual one-dimensional oscillators. Each of the latter spectra can be expressed analytically and follow a Poisson distribution of intensity.[7] The resulting stick spectrum thus obtained is again convoluted with a Lorentzian function with a full-width at the half-maximum (fwhm) of 10 meV to calculate the spectral envelope. The spectrum reveals a dominant excitation of ν_1 and ν_2 modes, the first two peaks from the 0−0 line. These peaks are ∼153 and ∼190 meV spaced in energy, corresponding to the frequency of ν_1 and ν_2 modes, respectively, in the cationic ground state. The next three peaks correspond to the excitation $2\nu_1$, $\nu_1 + \nu_2$, and $2\nu_2$, respectively. The remaining high-energy peaks correspond to the excitation of higher quanta of ν_1 and

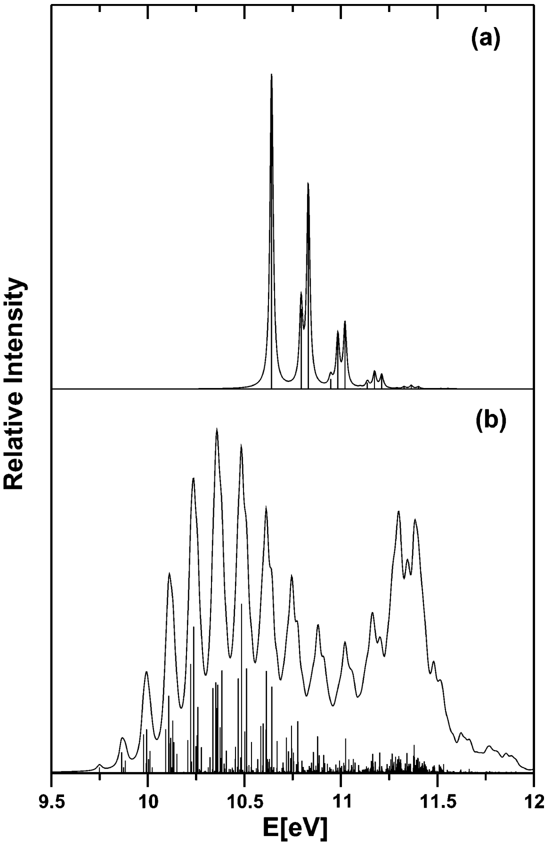

Figure 6. Photoelectron band of the $\tilde{X}^2E'$ electronic manifold of CP$^+$ computed with three totally symmetric modes (ν_1−ν_3) and three degenerate (ν_4−ν_6) modes alone, within the linear vibronic coupling scheme, is shown in panels (a) and (b), respectively. Each theoretical stick spectrum is convoluted with the Lorentzian function of 10 meV fwhm to calculate the spectral envelope.

ν_2 and to combination modes. The excitation of the ν_3 vibrational mode is negligibly small (the intensity is 10^3 times less than the 0−0 line) and is not visible in the spectrum. The peaks in the spectrum are weighted by the coupling strength, $\kappa^2/2\omega^2$ (Poisson parameter), of the respective vibrational mode, which yields the intensity of the fundamental relative to the 0−0 line.

In Figure 6b the spectrum obtained with the degenerate vibrational modes ν_4, ν_5, and ν_6 and a linear vibronic coupling scheme is shown. The stick spectrum is calculated with 40, 40, and 8 harmonic oscillator basis functions along each component of these degenerate modes. The calculations are carried out in a complex basis representation using complex coordinates for the degenerate vibrational modes to take advantage of the 3-fold symmetry of the system.[7] This leads to a secular matrix of dimension 33,359,445, which is diagonalized using 15,000 Lanczos iteration steps. The resulting stick spectrum is convoluted with a Lorentzian function of 10 meV fwhm to calculate the spectral envelope.

The convergence of the stick spectrum is explicitly checked with respect to the size of the basis set as well as the number of Lanczos iteration steps. A careful inspection of the spectral intensity and the coupling strengths of the vibrational modes ν_4, ν_5, and ν_6 reveal dominant excitations of ν_4 and ν_5 modes in the spectrum. Line spacings of ∼114, ∼134, and ∼184 meV corresponding to the excitation of ν_4, ν_5, and ν_6 vibrational modes can be observed from the spectrum. The latter is very weakly excited, which is also indicated by its extremely small coupling strength. The clumping of spectral lines under each peak and a huge line density is indicative of strong coupling JT effects due to the vibrational modes ν_4 and ν_5. This increases the line density in the spectrum, and for energies below ∼11 eV leads to a long series of resonances corresponding to vibrational motion on the lower JT sheet $\mathscr{V}_-$. For energies above ∼11 eV also $\mathscr{V}_+$ plays a role. The strong nonadiabatic effects, however, mix the discrete vibrational levels of $\mathscr{V}_+$ with the quasi-continuum levels of $\mathscr{V}_-$, and therefore, the nuclei undergo simultaneous transitions to both sheets of the JT split PES. The occurrence of higher energy maxima in the spectral envelope is thus explained to be due to the metastable resonances of the upper potential well. The latter is very narrow and extremely anharmonic and as a result its lowest levels are widely spaced in energy. These are showing up in the spectral envelope of Figure 6b in the energy range above 11 eV: between ∼11 and 11.5 eV the resonance corresponds to the ground vibrational level of $\mathscr{V}_+$ while around 11.8 eV another structure becomes visible which represents the first excited vibrational level of $\mathscr{V}_+$. The broadening mechanisms are just the strong nonadiabatic coupling effects characteristic for Jahn−Teller intersections.[16] These are referred to as Slonczewski resonances and the existence of these resonances was demonstrated in several model (E × e)−JT problems.[9,48,49]

The complete photoelectron band of the electronic ground state of CP$^+$ obtained with the linear vibronic coupling scheme is shown in Figure 7b along with the experimental result of Holland and co-workers in Figure 7a. The theoretical stick spectrum in Figure 7b is obtained by convoluting the two partial stick spectra in Figure 6a,b. Because of this convolution, the progression of the symmetric mode spectrum is represented on each JT line of Figure 6b. The resulting convoluted stick spectrum is then convoluted again with a Lorentzian function of 10 meV fwhm to generate the spectral envelope shown in Figure 7b. A comparison of this theoretical envelope with the experimental one in Figure 7a reveals a very good overall agreement between the two. The overall width of the theoretical spectrum is in good accord with the experimental one. The splitting between the two maxima of the theoretical spectrum of ∼0.76 eV compares well with its experimental value of ∼0.78 eV. The progression in the low-energy wing of the envelope is mainly formed by the JT active ν_4 and ν_5 vibrational modes. The spacing between the successive peaks in the theoretical envelope is ∼40 meV higher than its experimentally reported average value of ∼60 meV. We, however, note that the experimental band is smoothed and it is not clear at this point if the line spacings are affected in this smoothening procedure. In fact, the structure present in the second maximum of the theoretical envelope is not seen in the experimental result. Apart from these discrepancies, the regularity in the low-energy progression is nicely reproduced by the theoretical result. When compared with the pure JT spectrum of Figure 6b, it can be seen that the symmetric vibrational modes cause additional broadening of the spectral envelope and some of the low-energy structures are quenched.

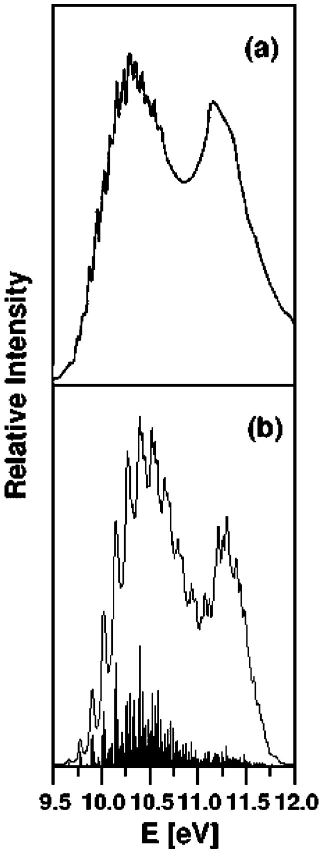

Figure 7. Comparison of the experimental (ref 27) and final theoretical (of the linear vibronic coupling model) results for the $\tilde{X}^2E'$ photoelectron band of CP$^+$. The theoretical stick spectrum is obtained by convoluting the two partial spectra of Figure 7a,b. The resulting complete stick spectrum is again convoluted with a Lorentzian of 10 meV fwhm to calculate the spectral envelope. The theoretical spectrum is shifted by 0.062 eV to the higher energy along the abscissa to reproduce the adiabatic ionization position of the band at its experimental value.

We now discuss the effect of second-order coupling on the above theoretical spectra. In Figure 8 we show the two partial spectra obtained with the symmetric (panel a) and JT active (panel b) vibrational modes. The complete spectrum obtained by convoluting these two partial spectra is shown in Figure 8c. The size of the vibrational basis, number of Lanczos iterations, and the convolution width of the Lorentzian are the same as those described for the spectra shown in Figures 6a, 6b, and 7b. A close look at the quadratic symmetric mode spectrum in Figure 8a reveals essentially no difference with that obtained

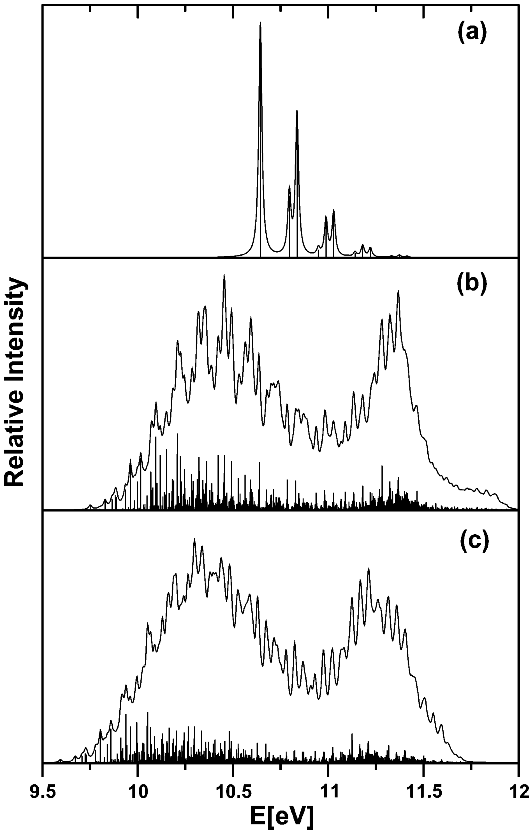

Figure 8. Photoelectron band of the $\tilde{X}^2E'$ electronic manifold of CP^+ calculated with the quadratic coupling scheme (see text for details). The intensity (in arbitrary units) is plotted as a function of the energy of the final vibronic states. The spectrum calculated with the symmetric ($\nu_1-\nu_3$) modes and the JT ($\nu_4-\nu_7$) modes alone is shown in panels (a) and (b), respectively. These two partial spectra of panels (a) and (b) are convoluted to generate the complete spectrum of panel (c). The theoretical stick spectrum of each panel is convoluted with the Lorentzian function of 10 meV fwhm to generate the corresponding spectral envelope. To have a clearer representation, the stick spectra in panels (b) and (c) are magnified by a factor of 3.

with the linear coupling scheme (cf. Figure 6a). The peaks are ~152 and ~192 meV spaced in energy corresponding to the frequencies of ν_1 and ν_2 vibrational modes modified by the respective second-order coupling terms (cf. Table 2).

The quadratic JT mode spectrum in Figure 8b, on the other hand, differs considerably from the linear one (cf. Figure 6b). Each peak of the linear spectrum is further split in the quadratic coupling scheme. Because of the increase of the line density, the quadratic JT spectrum is somewhat more diffuse. The apparent regularity in the low-energy progression is lost in the quadratic JT spectrum. The higher energy maxima appearing at 11.3 and 11.8 eV in Figure 8b, however, survive in the quadratic model. As discussed in relation to Figure 6b, these represent the first and second Slonczewski resonances. The above symmetric and the JT mode spectra are convoluted and the resulting composite spectrum is shown in Figure 8c. The overall appearance of the composite spectrum looks similar to the one obtained with the linear vibronic coupling scheme (cf. Figure 7b). In both cases, in particular, the second Slonczewski resonance at 11.8 eV is blurred by the convolution (cf. Figure 7b with 6b and Figure 8c with 8b) while the first one at 11.3 eV becomes broadened but still dominates the high-energy spectral profile. Thus, the first PE band of cyclopropane represents a prominent example of such a resonance in an actual molecular JT spectrum.

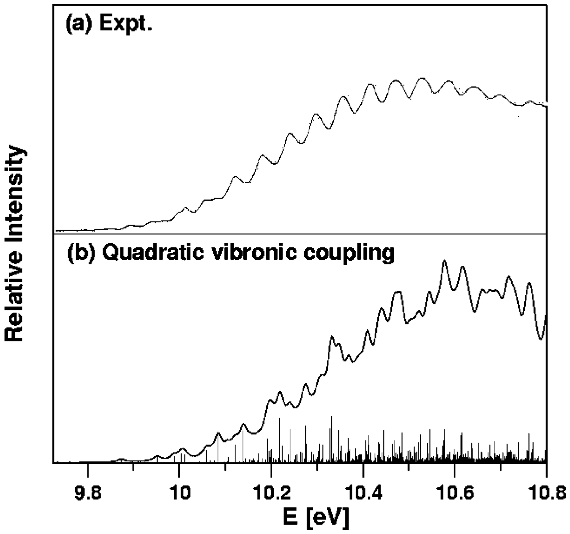

Figure 9. Low-energy wing of the $\tilde{X}^2E'$ photoelectron band of CP^+. The experimental result of Holland and co-workers[27] is shown in panel (a). The theoretical result of Figure 8c is reproduced in panel (b) to clearly reveal the impact of quadratic coupling terms on the low-energy progression in the band.

However, a more detailed analysis of the spectrum in Figure 8c reveals a dramatic effect of the quadratic JT coupling parameters on the vibronic fine structure of the photoelectron band. To reveal this more clearly, we present in Figure 9 an enlarged view of the low-energy part of Figure 8c (in panel b) along with the experimental data (in panel a). A comparison of the two results indicates that the quadratic JT coupling does account for a lower value (<100 meV) of the average spacing of this low-energy progression. An average spacing of the order of ~ 60 meV can be estimated from the quadratic vibronic coupling result. However, the apparent irregularity in the vibronic structure of the quadratic coupling results when compared to the linear coupling and the experimental results are not clear at the moment. It is also not clear if the smoothening procedure applied to the experimental results causes any reduction of the irregularity. It is to be noted that the apparent regularity of the experimental result may also be due to the usual poor energy resolution of the photoelectron spectrometer. More work to unravel this issue considering intermode coupling terms and also the possible effects due to the double-prime vibrational modes and the effect of the next excited electronic states is presently underway.

V. Summary and Outlook

We have presented a detailed theoretical account of the static and dynamic aspects of the (E × e)−JT interactions in the degenerate $\tilde{X}^2E'$ electronic ground state of CP^+. The vibronic structure of this electronic state is calculated with the aid of an ab initio based quantum dynamical approach and compared with the lowest photoelectron band of CP recorded most recently by Holland and co-workers using He I and synchrotron radiation as excitation sources.

In our theoretical approach we employed a model diabatic Hamiltonian within linear and quadratic vibronic coupling schemes. The equilibrium geometry of CP in its ground electronic state is optimized at the MP2 level of theory and the harmonic force field and the dimensionless normal coordinates are calculated. The equilibrium geometry parameters and the harmonic vibrational frequencies thus obtained are in close agreement with the experimental findings. The vertical ionization energies of CP^+ are calculated as a function of the normal mode displacements from the equilibrium geometry by the outer valence Green's function method. These energies are equated with the adiabatic potential energies of the $\tilde{X}^2E'$ electronic state of CP^+ and fitted analytically to the adiabatic form of the model diabatic Hamiltonian (eqs 5−9) to derive the relevant coupling parameters.

The experimentally recorded lowest photoelectron band of CP revealed a twin structure with a resolved regular progression in the low-energy wing of the first maximum and a highly diffuse structure of the second maximum. The separation between the two maxima of this twin band is reported to be ∼0.78 eV. An average spacing of peaks in the low-energy wing of ∼60 meV, attributed mainly to the CH_2 wagging mode, was also reported. In our theoretical approach we systematically examined the vibronic structure of this twin band. The coupling parameters of the relevant vibrational modes revealed that the symmetric vibrational modes ν_1 (C−C stretching) and ν_2 (CH_2 scissoring) and the JT active vibrational modes ν_4 (CH_2 wagging), ν_5 (ring deformation), and ν_6 (CH_2 scissoring) are only excited in the photoelectron transition. Out of the above three JT active modes only two, ν_4 and ν_5, lead to strong first-order coupling and form progressions in the photoelectron band.

We considered these vibrational modes in the nuclear dynamical simulations. This makes the dynamical problem an eight-dimensional one involving two electronic states. Because of the nature of the $(E \times e)$−JT Hamiltonian (eqs 5−9), in the absence of any bilinear coupling terms, the symmetric and the JT modes are separately treated in the nuclear dynamics. We first analyzed the underlying vibronic structure of the twin band employing a linear vibronic coupling scheme. The results thus obtained are in very good overall agreement with the experimental data, indicating strong coupling JT effects of the ν_4 and ν_5 vibrational modes which lead to the appearance of two distinct maxima in the photoelectron band. The overall width of the twin band and the separation between the two maxima of ∼0.76 eV are reproduced nicely by the linear coupling scheme. Apart from these, the higher order JT resonances of the upper adiabatic cone are also resolved in the present study. With regard to the finer details, the average spacing in the low-energy progression of the photoelectron band estimated from the theoretical results is ∼40 meV higher than the experimentally reported value. Furthermore, the theoretical band for the second maximum of the bimodal profile is less diffuse than the experimental one.

To account for this discrepancy, we extended the vibronic coupling model by including the quadratic coupling terms. The results obtained from this approach qualitatively remain similar to the linear coupling results. Quantitatively, each peak in the low-energy wing is further splitted and the apparent regularity of the progression is lost. The average spacing between the peaks may be considered to be further reduced to ∼60 meV.

The above minor discrepancies between theory and experiment are to be attributed to the uncertainties in the estimate of the coupling parameters of the Hamiltonian, neglect of any bilinear coupling terms, and the possible role of double-prime vibrational modes, the energy resolution, and to the finite background that is latent in the experimental spectrum. We also note that the experimental spectrum is smooth and it is not clear if some discrepancies arise from this procedure. Apart from the above issues, the pseudo-Jahn−Teller (PJT) coupling to the next higher $\tilde{A}^2E''$ electronic state through the A', A''_2 and E'' vibrational modes may also have an influence on the fine structure of the twin band. We, however, note that the PJT coupling is less likely to alter the structure of the low-energy progression. An analysis of the effects of bilinear coupling terms and the PJT coupling to the $\tilde{A}^2E''$ electronic state on the $\tilde{X}^2E'$ photoelectron band is currently underway and is the subject of a forthcoming publication.

Acknowledgment. This study is in part supported by a research grant from the Volkswagen Stiftung under the partnership program. S.M. is a recipient of the Friedrich Wilhelm Bessel Forschungspreis of the Alexander von Humboldt foundation.

References and Notes

(1) Jahn, H. A.; Teller, E. *Proc. R. Soc. London, Ser. A* **1937**, *161*, 220.

(2) Öpik, U.; Pryce, M. H. L. *Proc. R. Soc. London, Ser. A* **1957**, *238*, 425. Longuet-Higgins, H. C.; Öpik, U.; Pryce, M. H. L.; Sack, R. A. *Proc. R. Soc. A.* **1958**, *244*, 1. Longuet-Higgins, H. C. *Adv. Spectrosc.* **1961**, *2*, 429.

(3) Huheey, J. E.; Keiter, E. A.; Keiter, R. L. *Inorganic Chemistry: Principles of Structure and Reactivity*, 4th ed.; Harper Collins: New York, 1993.

(4) Kaplan, M. D.; Vekhter, B. G. *Cooperative Phenomena in Jahn−Teller Crystals*; Plenum: New York, 1995.

(5) Sturge, M. D. *Solid State Phys.* **1967**, *20*, 91.

(6) Falvello, L. R. *J. Chem. Soc., Dalton Trans.* **1997**, *23*, 4463.

(7) Köppel, H.; Domcke, W.; Cederbaum, L. S. *Adv. Chem. Phys.* **1984**, *57*, 59.

(8) Köppel, H. *Z. Phys. Chem.* **1997**, *200*, 3.

(9) Bersuker, I. B.; Polinger, V. Z. *Vibronic Interactions in Molecules and Crystals*; Springer-Verlag: Berlin, 1989.

(10) Englman, R. *The Jahn−Teller Effect in Molecules and Crystals*; Wiley: New York, 1972.

(11) Miller, T. A.; Bondybey, V. E. In *Molecular Ions: Spectroscopy, Structure, and Chemistry;* Miller, T. A., Bondybey, V. E., Eds.; North-Holland: Amsterdam, 1983. Barckholtz, T. A.; Miller, T. A. *J. Phys. Chem. A* **1999**, *103*, 2321.

(12) Chancey, C. C.; O'Brien, M. C. M. *The Jahn−Teller Effect in C_{60} and Other Icasahedral Complexes*; Princeton University Press: Princeton, NJ, 1997.

(13) (a) Mahapatra, S.; Cederbaum, L. S.; Köppel, H. *J. Chem. Phys.* **1999**, *111*, 10452. (b) Mahapatra, S.; Worth, G. A.; Meyer, H.-D.; Cederbaum, L. S.; Köppel, H. *J. Phys. Chem. A* **2001**, *105*, 5567. (c) Döscher, M.; Köppel, H.; Szalay P. G. *J. Chem. Phys.* **2002**, *117*, 2645. (d) Köppel, H.; Döscher, M.; Bâldea, I.; Meyer, H.-D.; Szalay P. G. *J. Chem. Phys.* **2002**, *117*, 2657. (e) Woywod, C.; Scharfe, S.; Krawczyk, R.; Domcke, W.; Köppel, H. *J. Chem. Phys.* **2003**, *118*, 5880. (f) Mahapatra, S.; Vallet, V.; Woywod, C.; Köppel, H.; Domcke, W. *Chem. Phys.*, submitted for publication.

(14) Bersuker I. B. *Chem. Rev.* **2001**, *101*, 1067.

(15) Teller, E. *J. Phys. Chem.* **1937**, *41*, 109. Herzberg G.; Longuet-Higgins, H. C. *Discuss. Faraday Soc.* **1963**, *35*, 77. Carrington, T. *Discuss. Faraday Soc.* **1972**, 53, 27. Yarkony, D. R. *Acc. Chem. Res.* **1998**, *31*, 511. Robb, M. A. *Pure Appl. Chem.* **1995**, *67*, 783. Bernardi, F.; Olivucci, M.; Robb, M. A. *Chem. Soc. Rev.* **1996**, *25*, 321. Papers on conical intersections in photochemistry, spectroscopy, and chemical dynamics: *Chem. Phys.* **2000**, *259*, 121−337.

(16) *Conical Intersections: Electronic Structure, Dynamics and Spectroscopy*; Domcke, W., Yarkony, D. R., Köppel, H., Eds.; World-Scientific: Singapore, 2004 (in press).

(17) Herzberg, G. *Molecular Spectra and Molecular Structure*; Van Nostrand: New York, 1966; Vol. 3.

(18) Köppel, H.; Cederbaum, L. S.; Domcke, W. *J. Chem. Phys.* **1988**, *89*, 2023. Mahapatra, S.; Köppel, H. *J. Chem. Phys.* **1998**, *109*, 1721. Köppel, H.; Döscher, M.; Mahapatra, S. *Int. J. Quantum Chem.* **2000**, *80*, 942.

(19) Leng, F. J.; Nyberg, G. L. *J. Electron Spectrosc. Relat. Phenom.* **1977**, *11*, 293.

(20) Basch, H.; Robin, M. B.; Kuebler, N. A.; Baker, C.; Turner, D. W. *J. Chem. Phys.* **1969**, *51*, 52.

(21) Turner, D. W.; Baker, C.; Baker, A. D.; Brundle, C. R. *Molecular Photoelectron Spectroscopy*; Wiley: New York, 1970.

(22) Kimura, K.; Katsumata, S.; Achiba, Y.; Yamazaki, T.; Iwata, S. *Handbook of HeI Photoelectron Spectra of Fundamantal Organic Molecules*; Japan Scientific Societies Press: Tokyo, 1981.

(23) Schweig, A.; Thiel, W. *Chem. Phys. Lett.* **1973**, *21*, 541.

(24) Lindholm, E.; Fridh, C.; Åsbrink, L. *Faraday Discuss. Chem. Soc.* **1972**, *54*, 127.

(25) Potts, A. W.; Streets, D. G. *J. Chem. Soc., Faraday Trans. 2* **1974**, *70*, 875.

(26) Keller, P. R.; Taylor, J. W.; Carlson, T. A.; Whitley, T. A.; Grimm, F. A. *Chem. Phys.* **1985**, *99*, 317.

(27) Holland, D. M. P.; Karlsson, L.; Siegbahn, K. *J. Electron Spectrosc. Relat. Phenom.* **2002**, *125*, 57.

(28) Haselbach, E. *Chem. Phys. Lett.* **1970**, *7*, 428.

(29) Müller-Dethlefs, K.; Peel, J. B. *J. Chem. Phys.* **1999**, *111*, 10550.

(30) Gleiter, P. *Top. Curr. Chem.* **1979**, *86*, 197.

(31) Collins, J. R.; Gallup, G. R. *J. Am. Chem. Soc.* **1982**, *104*, 1530.

(32) Bouma, W. J.; Poppinger, D.; Radom, L. *Isr. J. Chem.* **1983**, *23*, 21.

(33) Koopmans, T. *Physica* **1934**, *1*, 104.

(34) von Niessen, W.; Cederbaum, L. S.; Kraemer, W. P. *Theor. Chim. Acta* **1977**, *44*, 85.

(35) Lichten, W. *Phys. Rev.* **1967**, *164*, 131. Smith, F. T. *Phys. Rev.* **1969**, *179*, 111. O'Malley, T. F. *Adv. At. Mol. Phys.* **1971**, *7*, 223. Pacher, T.; Cederbaum, L. S.; Köppel, H. *Adv. Chem. Phys.* **1993**, *84*, 293.

(36) Baer, M.; *Chem. Phys. Lett.* **1975**, *35*, 112. *Mol. Phys.* **1980**, *40*, 110.

(37) Perrin, M. H.; Gouterman, M. *J. Chem. Phys.* **1967**, *46*, 1019. van der Waals, J. H.; Berghuis, A. M. D.; de Groot, M. S. *Mol. Phys.* **1967**, *13*, 301. *Mol. Phys.* **1971**, *21*, 497. Stephens, P. J. *J. Chem. Phys.* **1969**, *51*, 1995. Zgierski, M. Z.; Pawlikowski, M. *J. Chem. Phys.* **1979**, *70*, 3444.

(38) Domcke, W.; Köppel, H.; Cederbaum, L. S. *Mol. Phys.* **1981**, *43*, 851.

(39) Cullum, J.; Willoughby, R. *Lanczos Algorithms for Large Symmetric Eigenvalue Problems*: Birkhäuser, Boston, 1985; Vols. 1 and 2.

(40) Köppel, H.; Domcke, W. In *Encyclopedia of Computational Chemistry*; Schleyer, P. V. R., Ed.; Wiley: New York, 1998, p 3166.

(41) Dunning, T. H., Jr. *J. Chem. Phys.* **1989**, *90*, 1007.

(42) Cederbaum, L. S. *J. Phys. B* **1975**, *8*, 290.

(43) von Niessen, W.; Schirmer, J.; Cederbaum, L. S. *Comput. Phys. Rep.* **1984**, *1*, 57.

(44) Frisch, M. J.; Trucks, G. W.; Schlegel, H. B.; Gill, P. M. W.; Johnson, B. G.; Robb, M. A.; Cheeseman, J. R.; Keith, T.; Peterson, G. A.; Montgomery, J. A.; Raghavachari, K.; Al-Laham, M. A.; Zakrzewski, V. G.; Ortiz, J. V.; Foresman, J. B.; Cioslowski, J.; Stefanov, B. B.; Nanayakkara, A.; Challacombe, M.; Peng, C. Y.; Ayala, P. Y.; Chen, W.; Wong, M. W.; Andres, J. L.; Replogel, E. S.; Gomperts, R.; Martin, R. L.; Fox, D. J.; Binkley, J. S.; Defrees, D. J.; Baker, J.; Stewart, J. P.; Head-Gordon, M.; Gonzales, C.; Pople, J. A. *Gaussian 98*, revision E.1; Gaussian, Inc.: Pittsburgh, PA, 1995.

(45) Nijveldt D.; Vos, A. *Acta Crystallogr.* **1988**, *B44*, 281.

(46) Cederbaum, L. S.; Domcke, W. *Adv. Chem. Phys.* **1977**, *36*, 205.

(47) Günthard, Hs. H.; Lord, R. C.; McCubbin, T. K., Jr. *J. Chem. Phys.* **1956**, *25*, 768.

(48) Slonczewski, J. C. *Phys. Rev.* **1963**, *131*, 1596. Slonczewski, J. C.; Moruzzi, V. L. *Physics* **1967**, *3*, 237.

(49) Habitz, P.; Schwarz, W. H. E. *Theor. Chim. Acta* **1973**, *28*, 267. Köppel, H.; Haller, E.; Cederbaum, L. S.; Domcke, W. *Mol. Phys.* **1980**, *41*, 669.